Acta Cryst. (1990). B46, 139–149

Interpretation of HREM Images of Mullite

BY S. HAMID RAHMAN AND H.-T. WEICHERT†

Institut für Mineralogie, Universität Hannover, Welfengarten 1, 3000 *Hannover* 1, *Federal Republic of Germany*

(*Received* 8 *June* 1989; *accepted* 13 *October* 1989)

Abstract

HREM images of 3:2 and 2:1 mullite were recorded with the electron beam parallel to [001] and [010]. Image simulations for the projection on (001), based on systematically derived structure models, show a correspondence between the vacancy arrangement and the intensity of the simulated contrast pattern. On the other hand, HREM image simulations for projections on (010) show no definite correspondence between the intensity of the contrast pattern and the arrangement of the vacancies. A semiquantitative determination of regions in the crystal structure with enhanced oxygen-vacancy concentration can therefore be performed only for the (001) projection. Image reconstruction for the *ac* plane, using only the diffuse-scattering components, allows the determination of the distribution of crystal areas deviating in composition from the average structure. The intensity of the bright spots appearing on the HREM images of the (010) projection is not only correlated with the concentration of vacancies on certain sites, but is also influenced by all the components that modulate the crystal structure.

1. Introduction

Mullite, $Al_2[Al_{2+2x}Si_{2-2x}]O_{10-x}$, is a nonstoichiometric silicate compound with x, the number of missing oxygen atoms per average unit cell, varying between 0·17 and 0·59 (Cameron, 1977). It is formed at atmospheric pressure and high temperatures (> 1400 K). For $x = 0$ the above formula represents the three polymorphic modifications sillimanite, andalusite and kyanite, which are at least partially structurally related to mullite. For $x = 1$ it gives the chemical composition of the assumed ι-Al_2O_3 phase (Saalfeld, 1962).

The average structure of the 3:2 Ge-mullite ($x = 0{\cdot}25$) was determined by Durovic & Fejdi (1976) and refined for the isomorphous Si-mullite by Saalfeld & Guse (1981). The crystal structure of the 2:1 mullite ($x = 0{\cdot}4$) was determined and refined by Burnham (1963, 1964) and Durovic (1969), respectively. Both structures (2:1 and 3:2 mullite) differ only in the occupancies of certain atom sites. The structure consists of chains of edge-sharing AlO_6 octahedra running parallel to the c axis. These chains are cross-linked by $(Si,Al)O_4$ tetrahedra forming double chains, which also run parallel to the c axis (Fig. 1). The symmetry of this structure belongs to the space group *Pbam*. The approximate lattice constants are $a = 0{\cdot}755$, $b = 0{\cdot}768$ and $c = 0{\cdot}288$ nm ($Z = 1$). The compositional variation in mullite resulting from the substitution of Si for Al leads to the existence of a composition-dependent number of oxygen vacancies (□): $2Si^{4+} + O^{2-} \longleftrightarrow 2Al^{3+} + \square$.

The structure analyses show that vacancies occur only at the tetrahedral linking positions (O_c, O_c^*) [atom symbols after Angel & Prewitt (1986)]. The loss of the fourth coordinating oxygen causes the two cations on the tetrahedral sites (Si,Al site) to

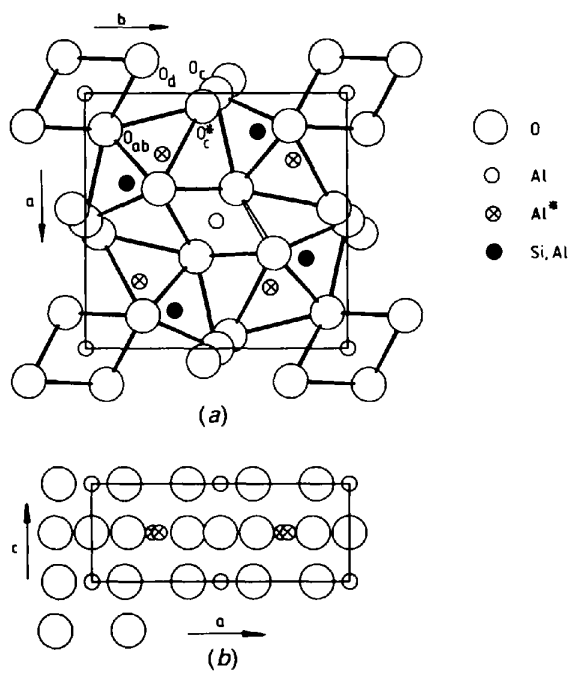

Fig. 1. Projection of the structure of mullite on (*a*) (001) and (*b*) (010).

† Present address: Nissei Sangyo GmbH, Hitachi Electronmicroscopy Department, Ross-Str. 74, 4000 Düsseldorf 30, Federal Republic of Germany.

0108-7681/90/020139-11$03.00

occupy the neighbouring positions of the second tetrahedral site denoted by Al* (Fig. 1). A re-examination of the average structure of 2:1 mullite, using third- and and fourth-order tensors to describe the very small displacements of the oxygen atoms O_{ab} and O_d owing to the occurrence of a vacancy or to the type of cation occupying the tetrahedral site was published by Angel & Prewitt (1986).

X-ray and TEM diffraction patterns of the *h*0*l*, 0*kl* and $hk\frac{1}{2}$ planes show diffuse streaks and satellite reflexions. Their appearance indicates a modulation within the mullite structure which doubles the *c* axis and has a composition-dependent, incommensurable periodicity along the *a* axis (Fig. 13). McConnell & Heine (1984, 1985) and Heine & McConnell (1984) carried out a group-theoretical analysis based on Landau theory in order to explain the origin of the incommensurability of the mullite structure. They derived two ordering schemes for mullite which have the symmetry of a pair of irreducible representations of the space group of the average structure (*Pbam*). The component structure, with Shubnikov symmetry $P_c nnm$, orders the vacancy distribution; the other, with Shubnikov symmetry $P_c bnm$, orders the aluminium and silicon atoms on the tetrahedral sites.

Using the method described by McConnell & Heine (1984), Angel & Prewitt (1987) calculated difference Patterson syntheses using the intensities of the satellite reflexions of a mullite with $x = 0{\cdot}4$. Assuming maximum ordering of the two component structures mentioned above they determined the approximate deviation of the occupancies for the Al*, (Si,Al), O_c and O_c^* sites from the average structure for the component structure with $P_c nnm$ symmetry.

High-resolution transmission electron microscopy (HREM) studies of mullite have been performed for crystals with $x \simeq 0{\cdot}4$ by Nakajima, Morimoto & Watanabe (1975) and for mullite with $x = 0{\cdot}48$ and $x = 0{\cdot}54$ by Ylä-Jääski & Nissen (1983). Nakajima *et al.* (1975) interpreted the white spots in the image as corresponding to low atomic density in the structure. The spot intensities are considered to be correlated to different oxygen removal and displacement of the cations in the tetrahedral sites along the *b* axis. Furthermore, they reported an increased concentration of oxygen vacancies arranged periodically in every third or fourth layer parallel to (100). In mullites with $x = 0{\cdot}48$ and $x = 0{\cdot}54$, Ylä-Jääski & Nissen (1983) observed the existence of antiphase domains with the antiphase boundaries parallel to (100) and slightly inclined against (601), respectively. Both HREM investigations were carried out with the electron beam parallel to the [010] zone axis. In this illumination direction many atoms overlap in the projection and the contrast change owing to the existence of oxygen vacancies cannot easily be determined (Eberhard, Hamid Rahman & Weichert, 1986). Furthermore, special attention has to be paid in the case of contrast simulations of structures involving point defects on special positions (Hamid Rahman, 1988*a*).

Recently Schryvers, Srikrishna, O'Keefe & Thomas (1988) examined 1·7:1 mullite ($x = 0{\cdot}32$) obtained by a sintering reaction between Al_2O_3 and $ZrSiO_4$. They reported a random distribution of the oxygen vacancies and concluded that the simulations of the *ab* plane, using an average structure model, rule out any direct correlation between the vacancy arrangement and the simulated contrast distribution.

In the present investigation HREM images were taken from very thin mullite crystals ($t = 2$–4 nm; $x = 0{\cdot}25$ and $0{\cdot}4$) with the electron beam parallel to the [001] and [010] zone axes. Using systematically developed structure models, an attempt is made to determine, at least semiquantitatively, the arrangement of the O vacancies by analyzing the observed differences of the image contrast of the *ab* plane. Moreover, image reconstruction procedures were carried out to determine the deviation from the average structure using only the diffuse-scattering component of the *h*0*l* plane.

2. Experimental

Several mullite crystals were grown using the solid-state reaction (sinter process) between quartz and γ-Al_2O_3. Stoichiometric, well-homogenized mixtures of the reactants ($3Al_2O_3.2SiO_2$) were pressed to tablets and sintered at temperatures in the range 1673–1873 K for 15–48 h. The lattice constants (after Cameron, 1977) and energy-dispersive X-ray analyses (Kevex 7000 EDX-spectrometer attached to a Hitachi S-530 scanning electron microscope) gave the chemical composition of 3:2 mullite with the formula: $Al_2[Al_{2\cdot5}Si_{1\cdot5}]O_{9\cdot75}$. The 2:1 mullite crystals investigated ($Al_2[Al_{2\cdot8}Si_{1\cdot2}]O_{9\cdot6}$) were commercially produced samples. They were kindly supplied by Dr H. Schneider (Bonn).

The crystals were crushed in alcohol using an agate mortar. The crystallites were then transferred onto a copper grid supporting a perforated carbon film.

A Hitachi H-800 TEM operating at 200 kV was used for the high-resolution observations. The microscope is equipped with a top-entry ultrahigh-resolution specimen-tilting stage ($\pm 10°$) and a high-brightness single-crystal LaB_6 cathode. The microscope constants used in the image simulations are listed in Table 1. For all images an objective aperture with a diameter of 25 μm was chosen. This is equivalent to $5{\cdot}5\ nm^{-1}$ in reciprocal space. The images were recorded either on photographic plates or in special cases (image reconstruction) by using a

Table 1. *Microscope constants* (*H*-800)

Acceleration voltage, U_0	200 kV
Wavelength, λ	0·0025097 nm
Spherical aberration, C_s	1 mm
Chromatic aberration, C_c	1·2 mm
Focus spread, Δ	5 nm
Divergence, α	5×10^{-4} rad

video unit connected to an image processing system. This system is connected to an array processor which allows a forward and backward Fourier transformation of a full frame (512 × 512 pixels) within a few seconds.

3. Structure models and image simulations

In order to interpret the experimental HREM images, computer image simulations were performed. The *n*-beam calculations for these image simulations were made using the multislice approximation developed by Cowley & Moodie (1957) and reviewed for numerical application by Goodman & Moodie (1974) and Cowley (1975).

The existence of point defects on special positions within the unit cell (O_c vacancies on $0,\frac{1}{2},\frac{1}{2}$ or $\frac{1}{2},0,\frac{1}{2}$) necessitates the use of supercells for the calculation of the Fourier coefficients of the scattering potential (periodic continuation). Hence, the use of occupancy factors whose values are not equal to one is avoided in the calculation of this potential. To yield the same resolution compared with simulations based on a normal unit cell ($1a \times 1b$) the number of interacting beams must be increased in the multislice calculations. For a supercell of the size ($2a \times 2b$) the number of beams must be increased by nearly a factor of four. This requires a large computer memory and takes long run times.

To avoid these disadvantages and to determine the relationship between the oxygen-vacancy distribution and the calculated contrast in a fast and reliable manner, the potential for the transmission function was calculated by applying a new method [the potential exchange method (Hamid Rahman, 1988*a*)]. In this method (Fig. 2) the potential of a defect-free unit cell and of a unit cell with periodically arranged defects is calculated. In both calculations the positions of the cations are occupied according to the desired nonperiodic unit cell *c* (Fig. 2). In the second step the values of the projected potential of a quarter of the unit cell (*a*) (shaded area) is exchanged with the values of the shaded area of unit cell (*b*) (Fig. 2). With this nonperiodic scattering potential the transmission function was calculated using the following Fourier integral:

$$Q(h,k) = \int_{x=0}^{1}\int_{y=0}^{1-\Delta y} \exp[-i\sigma\varphi_1(x,y)]\exp(i\Omega)\mathrm{d}x\,\mathrm{d}y + \int_{x=0}^{1}\int_{y=1-\Delta y}^{1} \exp[i\sigma\varphi_2(x,y)]\exp(i\Omega)\mathrm{d}x\,\mathrm{d}y \quad (1)$$

where $\varphi(x,y)$ is the scattering potential, σ is the interaction constant and $\Omega = 2\pi(hx + ky)$. For vacancies positioned on $0,\frac{1}{2},\frac{1}{2}$ the integral limits have to be changed.

The computational work was carried out on a CDC-Cyber 180-990S computer, using a program system developed at our institute for the HREM image simulations. 2401 beams were included in the multislice calculations, which gave a saturation of the accuracy. No absorption effects were taken into account. In the case of the beam direction parallel to [001], the *c*-lattice constant (0·288 nm) was chosen as slice thickness. For the beam direction parallel to [010], the length of the half unit cell (0·384 nm) was taken as slice thickness. According to the cut-off of the contrast transfer function, the final image simulations were carried out with 45 beams for unit cells of the size $1a \times 1b$ and with 17 beams for unit cells of the size $1a \times 1c$.

To find the most suitable projection plane for observing the oxygen vacancies in the structure of mullite, the oxygen packing projected on (001) and (010) was first considered. The projection on (001) is shown in Fig. 3. A striking feature of this projection is the appearance of channels beside the O_c atoms. They are drawn in black in parts of Fig. 3. The dotted lines in the lower right part of Fig. 3 represent the O_c and O_c^* positions which are occupied depending upon the occupancies of the (Al,Si) or Al* positions. The minimum distance of two neighbouring channels corresponds to the diameter of an oxygen atom and amounts to about 0·26 nm. Under appropriate illumination conditions these channels can be resolved. The existence of oxygen vacancies

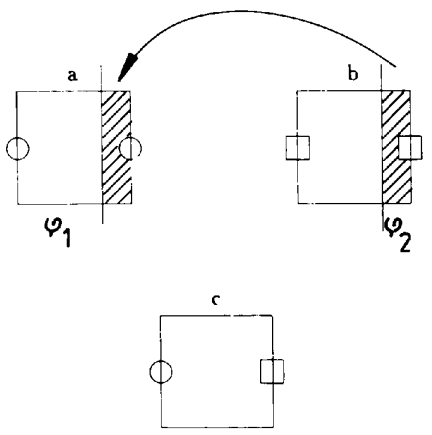

Fig. 2. Scheme showing the potential exchange method.

on the O_c site results in a large cavity between two unit cells. It is therefore expected that the local variation of the scattering potential owing to the existence of a vacancy causes a variation of the contrast pattern or, at least, its intensity.

A view of the oxygen packing of the mullite structure projected on (010) (Fig. 1*b*) shows that many atoms overlap. Hence, a simple relation between the image contrast and the arrangement of oxygen vacancies is not expected.

To enable any arrangement of vacancies along the *c* direction, the five basis structure models, shown in Fig. 4, were used for the contrast simulations. The vacancy-free model *e* resembles the structure of sillimanite. Based on the average structure of mullite, however, the O_c atoms in this model are situated on the edge of the unit cell unlike the positions of these atoms within the sillimanite structure (Taylor, 1928).

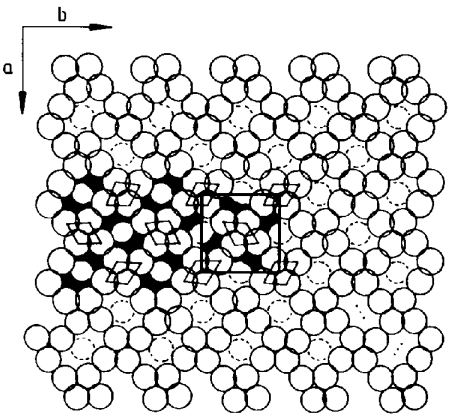

Fig. 3. Oxygen packing of mullite projected on (001).

Two series of HREM simulations for model *b* (Fig. 4) are given in Figs. 5 and 6. The transmission functions for these simulations were evaluated using a supercell (Fig. 5) and by the potential exchange method (Fig. 6). The contrasts were calculated for defocus values from −30 to −60 nm in 5 nm steps and for crystal thicknesses of 2·3, 3·4 and 5·7 nm. In these images and in all that will follow the *a* axis runs downwards and the *b* axis is horizontal. These simulations show that there are only negligible differences in the intensities of both simulation series, so that the less time-consuming potential exchange method, which in addition requires less computer memory, was used for most of the following calculations.

In each unit cell a pattern of four intensity maxima can be observed. In most of the simulations these maxima are diffuse. Only at defocus values of −50 and −55 nm can the four intensity maxima be clearly recognized. A comparison with the oxygen packing projected on (001) (Fig. 3) shows a correspondence between these maxima and the channels beside the O_c sites in the mullite structure. Based on this correspondence, further simulations were performed with defocus values of −50 nm and crystal thicknesses between 2·3 and 3·4 nm.

In order to examine the effect of contrast change caused by nonperiodic oxygen-vacancy arrangement along the *c* direction, images were calculated for some examples with different slice sequences (Fig. 7). As mentioned above it can be seen in every image that the four contrast maxima dominate at the defocus value used ($\Delta f = -50$ nm). The images in Figs. 7(*a–e*) show the simulations for the five basis structure models. In the simulations of the 'sillimanite'-like structure no visible differences of the

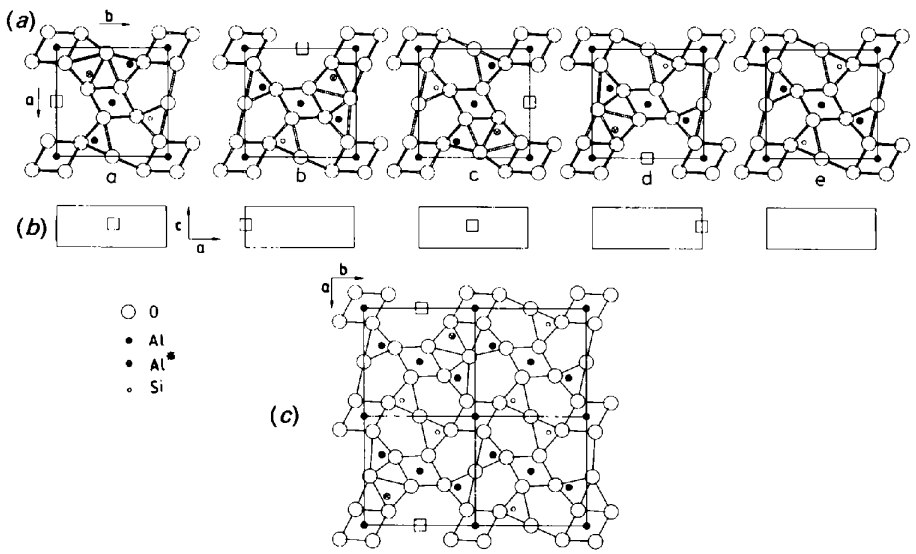

Fig. 4. Basis structure models for the image simulations: (*a*) projection on (001); (*b*) projection on (010) (only the positions of the vacancies □ are shown); (*c*) basis structure model *b* shown as a supercell.

intensities of the four maxima can be observed (Fig. 7*e*). On the other hand, the four intensity maxima of the simulations of the other four models (Figs. 7*a–d*) do not have the same intensity. Here the intensity value of the respective maximum, which is located clockwise next to the position of the projected defects, is strongly decreased. Though the existence of a vacancy channel parallel to [001] is rather non-realistic the above-described simulations show the relation between vacancy arrangement in the structure of mullite and contrast variation in HREM simulations. More runs with different slice sequences (listed in the caption of Fig. 7) confirmed this relation. In the simulations (Figs. 7*f–i*) two of the four maxima are less intense than the other maxima. Again, the less-intense maxima are located clockwise relative to the position of the defects. A four-slice run (Fig. 7*j*) in which a vacancy is positioned on each edge of the unit cell (slice sequence: *abcd*) shows no intensity differences between the four maxima. According to the calculated images (Fig. 7) it is evident that the contrast distribution of each unit cell is correlated with the corresponding vacancy arrangement along the cell edges.

In order to check if a simple relationship exists between the simulated contrast pattern of the *ac* plane and the arrangement of oxygen vacancies in the mullite structure, the images of different structure models were calculated. The results are shown in Fig. 8. In contrast to the image simulations for the *ab* plane, the *ac* image contrast does not show a one-to-one correspondence with the projected potential of the crystal structure. The positions of the intensity maxima change abruptly at rather small underfocus intervals. This is clearly visible in the simulation of the three structure models shown in

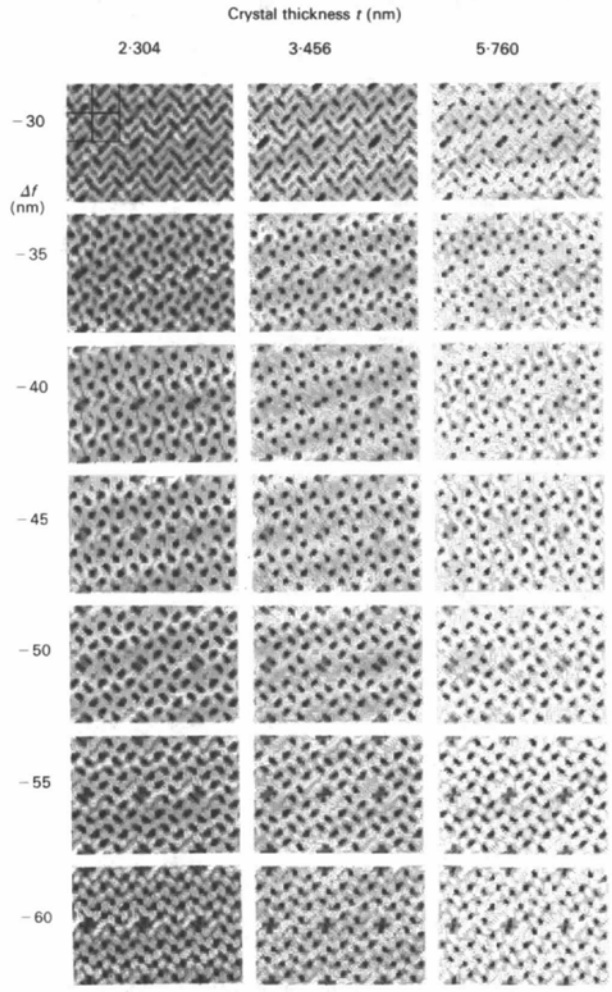

Fig. 5. HRTEM simulations for structure model *b* (Fig. 4). The transmission function was calculated using a supercell. Only the upper-left subcell should be compared with Fig. 6.

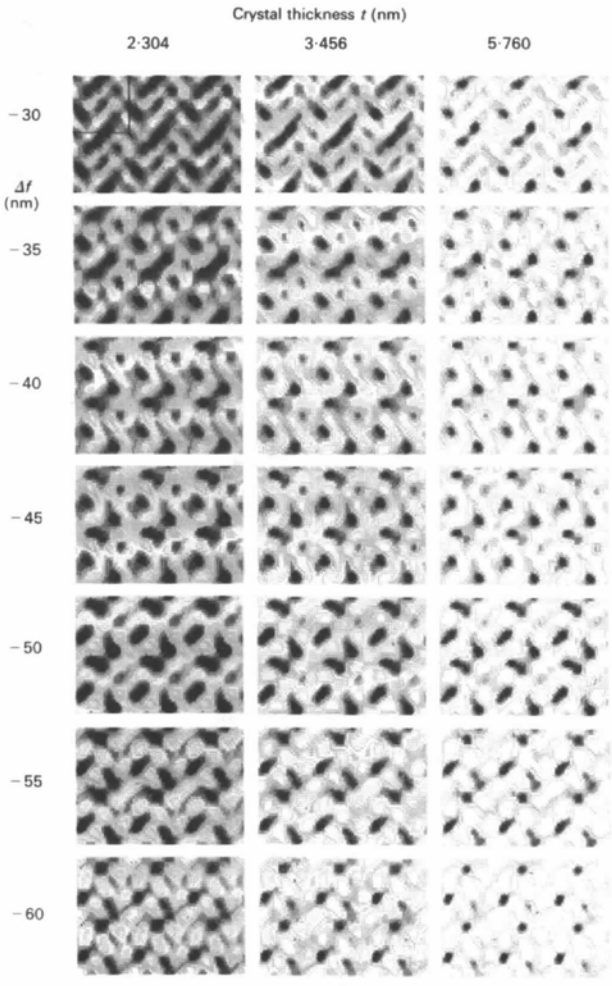

Fig. 6. HRTEM simulations for structure model *b* (Fig. 4). The transmission function was calculated by the potential exchange method.

Fig. 8 at defocus values of −55, −65 and −75 nm. However, an influence of the arrangement of vacancies on the calculated images can be observed. One of the resulting dots of the simulated contrast pattern shows a decreased intensity if vacancies exist in the structure model. However, in contrast to the pattern of the *ab* plane, a definite correspondence between the vacancy arrangement and intensity of the contrast pattern cannot be ascertained.

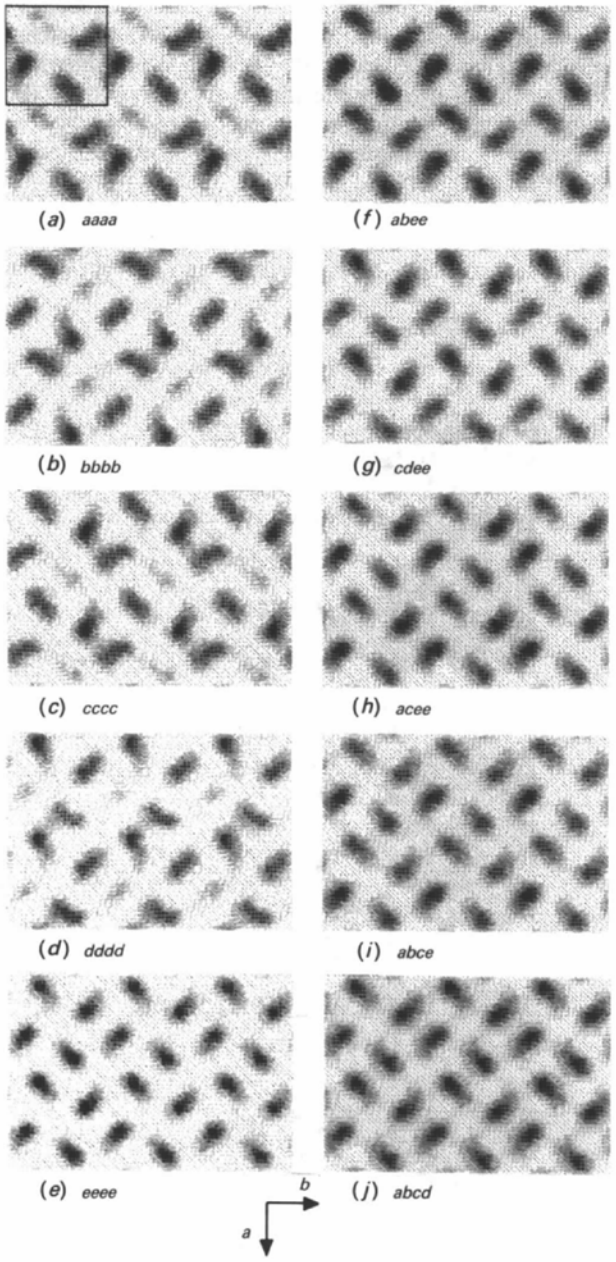

Fig. 7. Contrast simulations of the basis structure models (*a*)–(*e*) and of some models with different slice sequences (*f*)–(*j*). The slice sequences per cycle are given below each simulation. The letters correspond to the basis structure models shown in Fig. 4. The unit cell is outlined in (*a*). (Electron beam ‖[001]; crystal thickness: 2·4 nm; $\Delta f = -50$ nm.)

4. HREM images and discussion

To avoid kinematically and dynamically forbidden reflexions arising from the presence of glide planes in the mullite structure, some attention must be paid to crystal and beam alignement (Gjønnes & Moodie, 1965; Smith, Bursil & Wood, 1985; Self, Claisher & Spargo, 1985). The crystallites were carefully oriented in the microscope, so that the electron beam was parallel to the [001] or [010] zone axis. Current

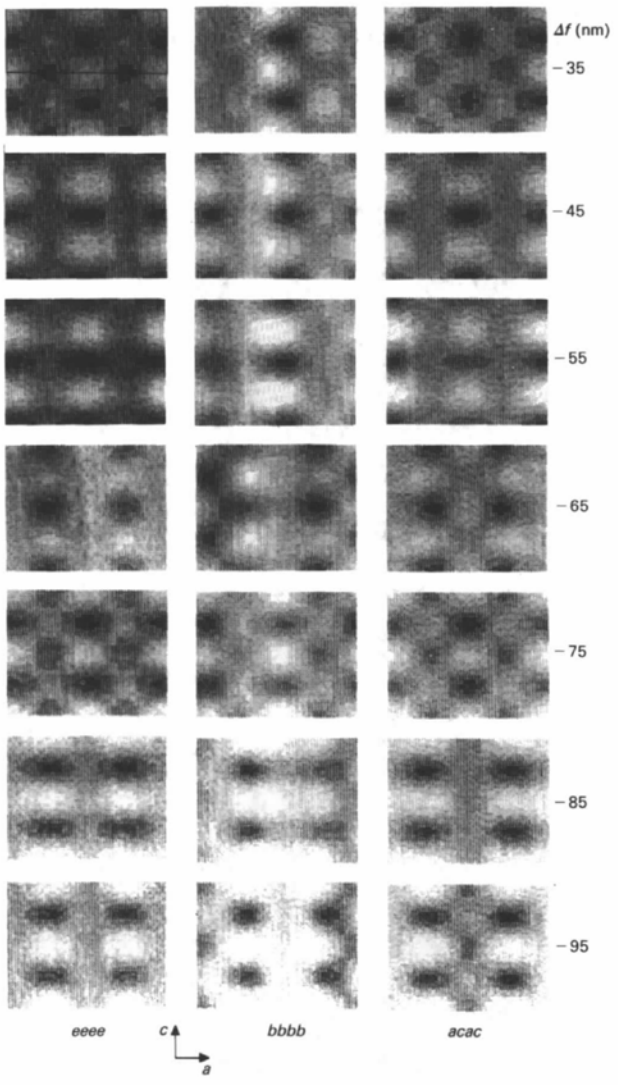

Fig. 8. Contrast simulations for three structure models. Electron beam ‖[010]. The slice sequences per cycle are given below each focus series. The letters correspond to the basis structure models shown in Fig. 4. (Crystal thickness: 3·07 nm.)

and voltage alignment were also performed to correct the beam tilt.

An HREM image for a very thin mullite crystal ($x = 0{\cdot}25$) is shown in Fig. 9. This image resembles the oxygen packing of the projected mullite structure (Fig. 3). The white spots in the experimental image correspond to the channels in the mullite structure (black in the packing model). Regions with minimum brightness (black in the reproduction) positioned between the white spots can be interpreted as the shadows of the AlO_6 octahedral columns. From the varying distances between these spots it can be assumed that the AlO_6 octahedra are slightly distorted. This observation is in accordance with the results of the structure refinement of Angel & Prewitt (1986).

The above interpretation of the experimental image is only possible because the crystal is very thin ($\simeq 2$ nm) and it behaves as a weak-phase object. In this case regions of low intensity in the image correspond to the projection of atom columns in the structure. The corresponding simulated image and the schematically drawn structure are shown as insets in Fig. 9.

Fig. 10(*a*) shows a wider area of the same crystal. A region of 80 unit cells is marked within this image. In each unit cell the same contrast pattern as obtained from the simulations (Figs. 5–7) can be observed. The strength of each of the four intensity maxima is, however, different from cell to cell. Applying the rules which describe the relationship between the strength of an intensity maximum and the concentration of vacancies (see §3) the vacancy distribution within these 80 unit cells was determined approximately. Fig. 10(*b*) shows a scheme of these 80 unit cells. The squares give the determined positions of increased vacancy concentration. It can be seen that regions with increased vacancy concentration alternate with areas of low vacancy concentration.

Fig. 11 shows an HREM image of mullite taken under a slight misalignment of the zone axis [001]. This axis was tilted approximately 1–2° around the [010] direction. In this image alternating darker and lighter contrast fringes can be observed. The repeat distance of these fringes is about $3a$. Their normal is tilted about 6° against [100], so the fringes have an approximate orientation parallel to (10.1.0). This observation is in agreement with the appearance of

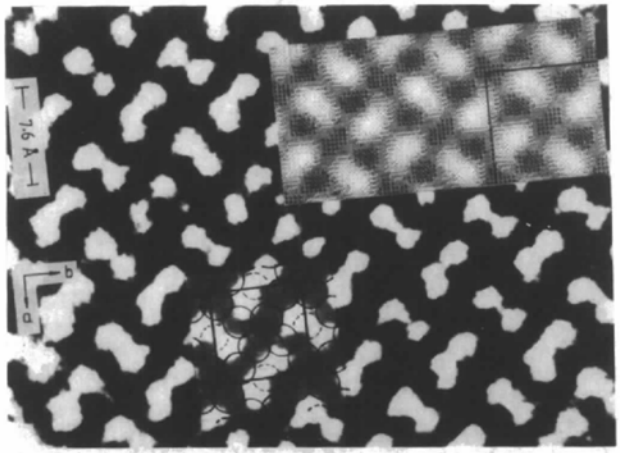

Fig. 9. HRTEM image of a very thin mullite crystal with a composition of $x = 0{\cdot}25$ (electron beam ||[001]). The simulated image ($\Delta f = 50$ nm, $t = 1{\cdot}7$ nm) and the projected oxygen packing are shown as insets.

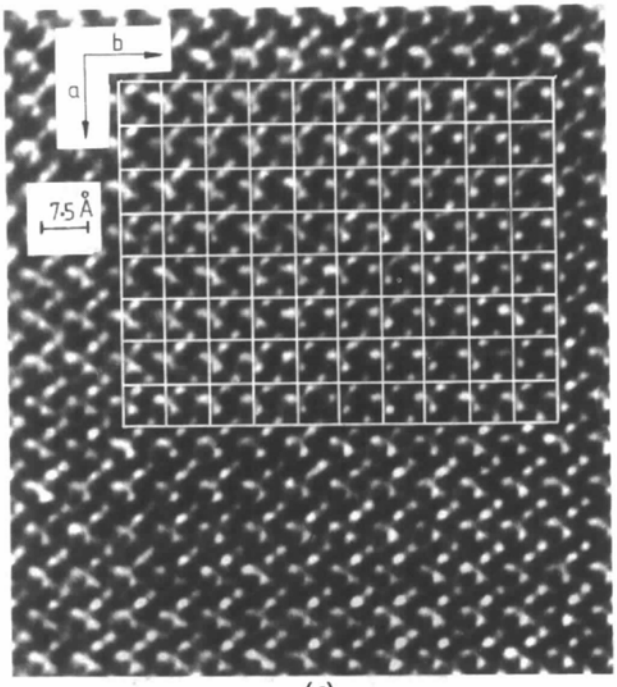

(*a*)

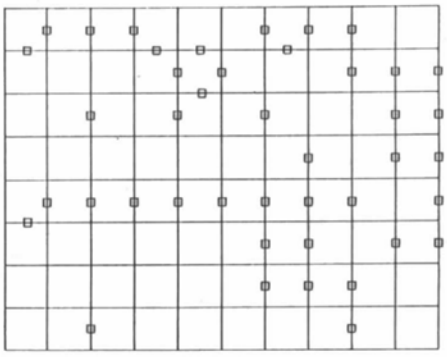

(*b*)

Fig. 10. (*a*) HRTEM image of the *ab* plane of mullite with a composition of $x = 0{\cdot}25$ ($\Delta f \simeq -50$ nm, $t \simeq 3{\cdot}4$ nm). An array of 80 unit cells is outlined ($a = 0{\cdot}75$ nm, $b = 0{\cdot}76$ nm). (*b*) Semiquantitative determination of sites with increased vacancy concentration (□).

the satellite reflexions within the a^*c^* plane and the distance between them ($\simeq \frac{2}{3}a^*$).

Similar contrast patterns were reported by Kumao, Nissen & Wessicken (1987). They observed such fringes on HREM images of plagioclases and they assumed that the reason for the existence of these patterns was the varying occupation of certain positions with Na and Ca atoms. In the case of mullite such a modulation would be caused by the alternating appearance of areas rich and poor in oxygen vacancies. However, it is very likely that this would happen only in Al-rich crystals. The fact that fringes appear irregularly (Fig. 11) leads to the assumption that mullite crystals consist of domains with varying Al concentration.

HREM imges of 3:2 and 2:1 mullite taken with the electron beam parallel to [010] and their corresponding diffraction patterns are shown in Figs. 12 and 13, respectively. It can be seen from the diffraction patterns that the intensity of the satellite and of the diffuse-scattering component increases with increasing Al concentration, which is equivalent to an increase of the vacancy concentration. Whereas the patterns in the image of the 3:2 mullite show only small intensity variations from unit cell to unit cell these variations are clearly marked in the image of the Al-rich 2:1 mullite. Additionally, dark stripes with an orientation approximately parallel to $(20\bar{1})$ and an average length of about 1·5 nm appear more clearly on the image of the 2:1 mullite.

The scattering potential $\varphi(x,y)$ of a disordered structure can be expressed as the sum of the average potential $\langle\varphi(x,y)\rangle$ and the deviation from this average potential $\Delta\varphi(x,y)$ (Cowley, 1975; Tanaka & Cowley, 1987):

$$\varphi(x,y) = \langle\varphi(x,y)\rangle + \Delta\varphi(x,y). \quad (2)$$

According to Heine & McConnell (1984) the second term can be split for incommensurate structures just

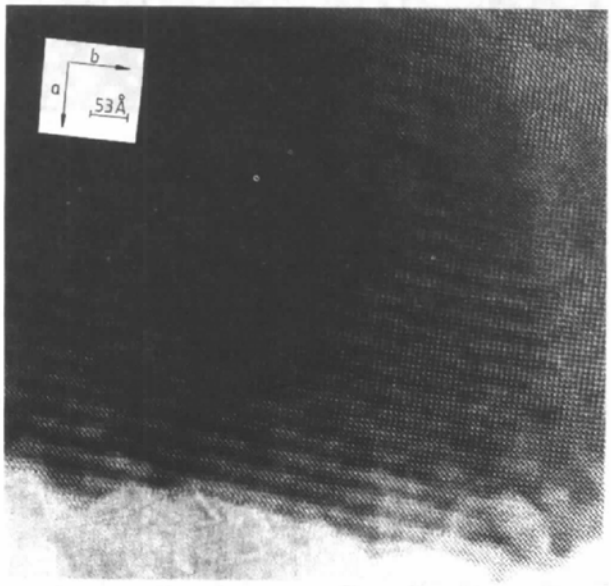

Fig. 11. HRTEM image of the *ab* plane of a slightly tilted mullite crystal ($x = 0{\cdot}25$). The [001] zone axis is tilted about 1–2° around the [010] direction. The repeat distance of the fringes is $\sim 3a$.

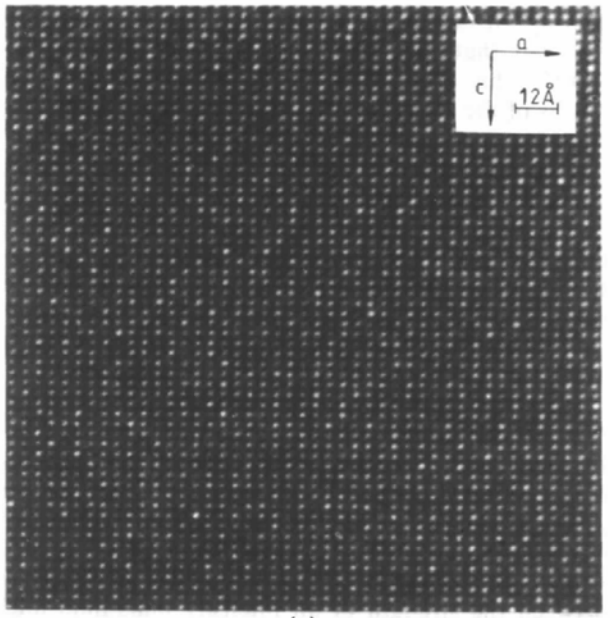

(*a*)

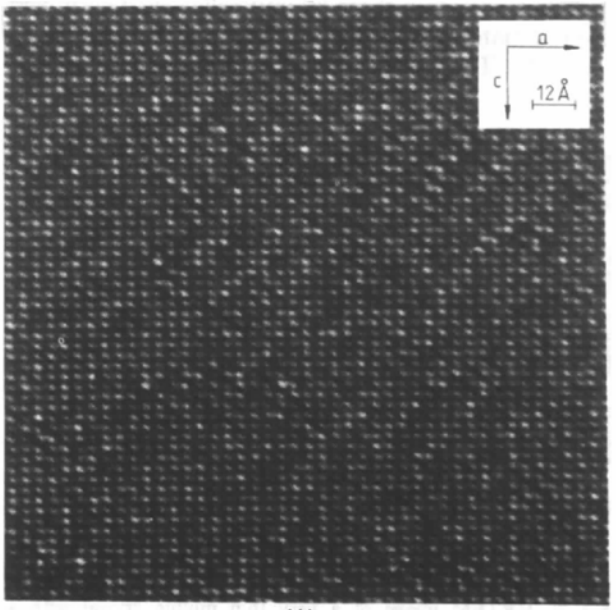

(*b*)

Fig. 12. HRTEM images of the *ac* plane for (*a*) $x = 0{\cdot}25$ and (*b*) $x = 0{\cdot}4$. Crystal thickness ~ 4 nm, $\Delta f = -55$ (5) nm.

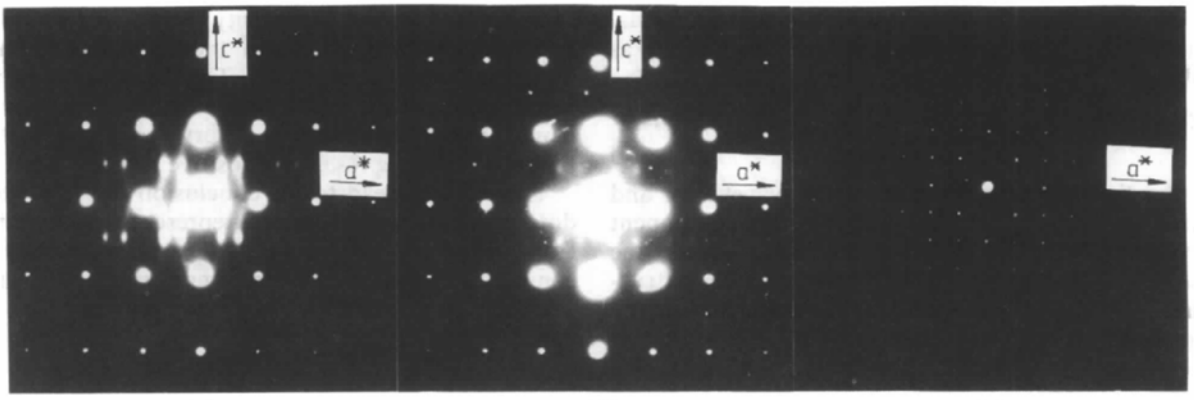

Fig. 13. Electron diffraction pattern of the *h*0*l* plane for (*a*) $x = 0{\cdot}4$ and (*b*) $x = 0{\cdot}25$, and (*c*) of the *hk*0 plane for $x = 0{\cdot}25$.

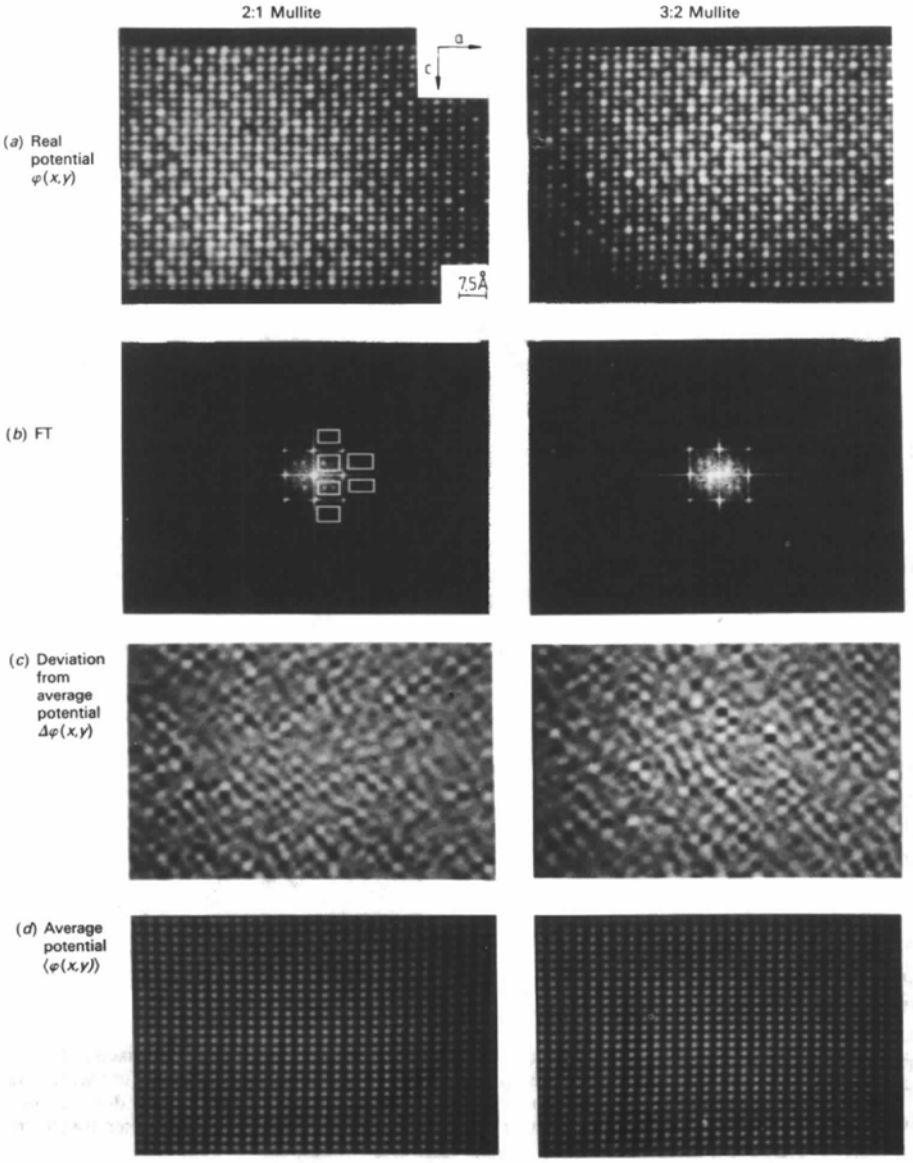

Fig. 14. Image reconstruction applied to two different HRTEM images of the *ac* plane for $x = 0{\cdot}25$ and $x = 0{\cdot}4$. (*a*) Digitized images (256 × 256 pixels). (*b*) Forward Fourier transformation of the sections shown in (*a*). (*c*) Backward Fourier transformation using the diffuse components marked in (*b*) (deviation from the average structure). (*d*) Backward Fourier transformation with Bragg reflexions only. Crystal thickness ≈ 4 nm; $\Delta f = -55$ (5) nm.

below the transition temperature into two sinusoidal terms. The real potential can then be written as follows:

$$\varphi(x,y) = \langle\varphi(x,y)\rangle + \Delta\varphi_1(x,y)\cos\mathbf{Qr} + \Delta\varphi_2(x,y)\sin\mathbf{Qr}. \quad (3)$$

In this formula **Q** is the modulation wavevector and **r** is a vector in real space. $\Delta\varphi_1(x,y)$ is the component structure which, in the case of the mullite, orders the vacancy distribution. The second component structure, $\Delta\varphi_2(x,y)$, orders the Si,Al distribution on the tetrahedral sites (McConnell & Heine, 1985).

In order to separate the average and deviation parts of the above formula, digitized HREM images of the *ac* plane (Fig. 14*a*) were Fourier-transformed using an array processor connected to the image processing system (Hamid Rahman, 1988*b*). The transformed crystal area consists of about 420 unit cells. The Fourier transforms are shown in Fig. 14(*b*). The image reconstructions were either performed only with Bragg reflexions [average structure, Fig. 14(*d*)] or only with the diffuse components within the marked area in Fig. 14(*b*) [deviations from the average structure, Fig. 14(*c*)]. Differences between the two images can only be observed in their digital Fourier transforms (Fig. 14*b*). Whereas the diffraction pattern of the 2:1 mullite shows clearly recognizable satellite reflexions, the diffraction pattern of the 3:2 mullite shows only diffuse maxima on the same positions. The backward Fourier transformations of the diffraction pattern, performed without the Bragg reflexions, give the deviations from the average potential. In both images the intensity maxima are coupled with intensity minima, which can be interpreted as relative, positive and negative deviations from the average structure. The Fourier transformations performed using only the Bragg reflexions give the expected equal contrast distribution of the average structure for both images.

In order to determine the defect distribution of a representative crystal area a wider section of a 2:1 mullite crystal ($\simeq$1700 unit cells; Fig. 15*a*) was examined by means of image-processing procedures. The image reconstruction with only the diffuse and the satellite reflexions gives the image shown in Fig. 15(*b*). The intensity of the white dots of this image (positive deviation) have been enhanced linearly in order to improve the surrounding contrast. The Fourier transformation of this image (Fig. 15*c*) gives a diffraction pattern similar to those obtained from electron or X-ray diffraction experiments (Figs. 13*a*,*b*). Hence, the intensity distribution of Fig. 15(*b*) represents the sum of the second and third terms of equation (3). It can be observed in Fig. 15(*b*) that most of the white dots are arranged in linear groups parallel to [102] or parallel to [001]. In the former direction the dots are spaced at an average distance of 0·47 nm (*i.e.* the periodicity length in this direction). In the [001] direction their average distance amounts to 0·56 nm (*i.e.* 2*c*). The distribution of the black dots, which result from negative deviations from the average structure, is very similiar to that of the white dots representing positive deviations.

These results lead to the conclusion that the white dots in Fig. 15(*b*) do indeed represent the deviation from the average structure. A separation of the two component structures (oxygen vacancies and

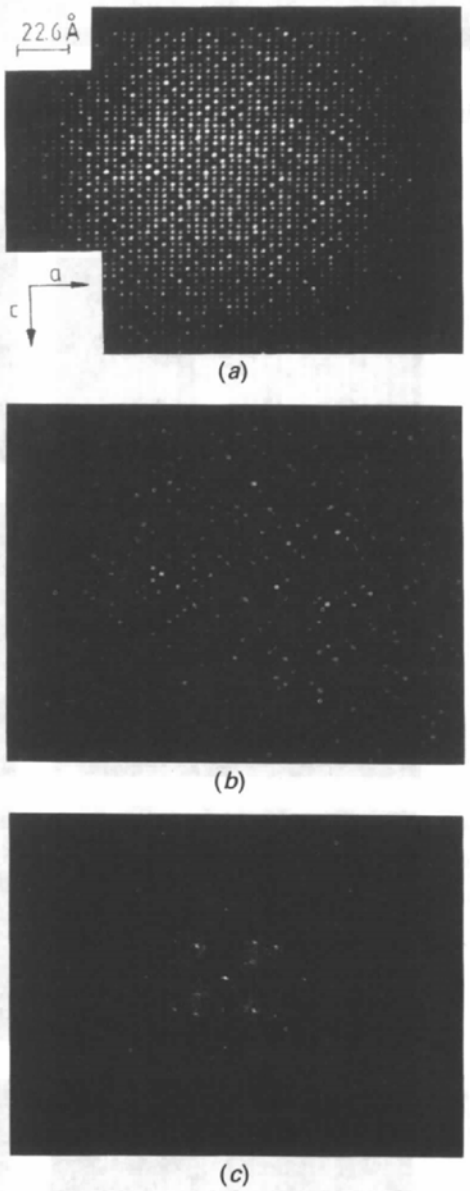

Fig. 15. (*a*) Full-frame digitized image (512 × 512 pixels) of a 2:1 mullite. (*b*) Image reconstruction using the diffuse-scattering components only. The intensity of the bright dots of this reconstruced image is linearly enhanced. (*c*) Fourier transform of (*b*). Crystal thickness $\approx$ 4 nm; $\Delta f = -55$ (5) nm.

'sillimanite'-like structure, respectively) is, however, not practicable. The dark regions within this image are assumed to be due to small domains possessing the average mullite composition. The average size of these domains is about 3·5 nm^2. They are separated by the above-mentioned, linearly arranged (parallel to [102]) white dots. An antiphase relationship between these domains cannot be confirmed for the mullite crystals investigated ($x = 0{\cdot}25$ and $x = 0{\cdot}4$).

The results discussed above show that the intensities of the white dots on the experimental HREM images of the *ac* plane are influenced by all components which modulate the structure of mullite. A proportionality between the intensity of these white dots and of only the concentration of vacancies on certain sites, as assumed by several authors (Nakajima *et al.*, 1975; Ylä-Jääski & Nissen, 1983), cannot be verified.

The assumption of Schryvers *et al.* (1988) that the oxygen vacancies are randomly distributed in mullite crystals obtained by sintering of $3Al_2O_3 + 2ZrSiO_4$ can be best verified by inspecting the b^*c^* and the a^*c^* diffraction pattern. In this case a continuous diffuse background rather than satellite reflexions must be obtained. Moreover, the computer simulations of Schryvers *et al.* (1988) along the *c* axis were unfortunately performed using an average structure model. According to our contrast calculations the intensity differences between the four contrast maxima within the unit cell must vanish owing to an equal vacancy distribution as shown in Fig. 7(*j*). The one-to-one correspondence between the HREM image contrast and the projected crystal structure of mullite, and the correspondence between the vacancy arrangement and the intensity of the simulated contrast features, can, according to the image simulations shown in Fig. 7, best be obtained on the (001) projections.

We thank Professor E. Eberhard for many helpful discussions and Dr H. Schneider (Bonn) for providing the 2:1 mullite single crystals. This work was supported by the Sonderforschungsbereich 173 of the Deutsche Forschungsgemeinschaft.

References

ANGEL, R. J. & PREWITT, C. T. (1986). *Am. Mineral.* **71**, 1476–1482.
ANGEL, R. J. & PREWITT, C. T. (1987). *Acta Cryst.* **B43**, 116–126.
BURNHAM, C. W. (1963). *Carnegie Inst. Washington Yearb.* **62**, 158–165.
BURNHAM, C. W. (1964). *Carnegie Inst. Washington Yearb.* **63**, 223–227.
CAMERON, W. E. (1977). *Am. Mineral.* **62**, 747–755.
COWLEY, J. M. (1975). *Diffraction Physics*. Amsterdam: North-Holland.
COWLEY, J. M. & MOODIE, A. F. (1957). *Acta Cryst.* **10**, 609–619.
DUROVIC, S. (1969). *Chem. Zvesti*, **23**, 113–128.
DUROVIC, S. & FEJDI, P. (1976). *Silikaty*, **20**, 97–112.
EBERHARD, E., HAMID RAHMAN, S. & WEICHERT, H.-T. (1986). *Z. Kristallogr.* **174**, 44–46.
GJØNNES, J. & MOODIE, A. F. (1965). *Acta Cryst.* **19**, 65–67.
GOODMAN, P. & MOODIE, A. F. (1974). *Acta Cryst.* A**30**, 280–290.
HAMID RAHMAN, S. (1988*a*). *Z. Kristallogr.* **186**, 113–116.
HAMID RAHMAN, S. (1988*b*). *Z. Kristallogr.* **186**, 116–119.
HEINE, V. & MCCONNELL, J. D. C. (1984). *J. Phys. C*, **17**, 1199–1220.
KUMAO, A., NISSEN, H.-U. & WESSICKEN, R. (1987). *Acta Cryst.* **B43**, 326–333.
MCCONNELL, J. D. C. & HEINE, V. (1984). *Acta Cryst.* A**40**, 473–482.
MCCONNELL, J. D. C. & HEINE, V. (1985). *Phys. Rev. B*, **31**, 6140–6142.
NAKAJIMA, Y., MORIMOTO, N. & WATANABE, E. (1975). *Proc. Jpn Acad.* **51**, 173–178.
SAALFELD, H. (1962). *Transactions of the* VIII *International Ceramic Congress, Copenhagen*, pp. 71–74.
SAALFELD, H. & GUSE, W. (1981). *Neues Jahrb. Mineral. Monatsh.* **4**, 145–150.
SCHRYVERS, D., SRIKRISHNA, K., O'KEEFE, M. A. & THOMAS, G. (1988). *J. Mater. Res.* **3**(6), 1355–1361.
SELF, P. G., CLAISHER, R. W. & SPARGO, A. E. C. (1985). *Ultramicroscopy*, **18**, 49–62.
SMITH, D. J., BURSIL, L. A. & WOOD, G. J. (1985). *Ultramicroscopy*, **16**, 19–32.
TANAKA, N. & COWLEY, J. M. (1987). *Acta Cryst.* A**43**, 337–346.
TAYLOR, W. H. (1928). *Z. Kristallogr.* **68**, 503–521.
YLÄ-JÄÄSKI, J. & NISSEN, H.-U. (1983). *Phys. Chem. Miner.* **10**, 47–54.

Acta Cryst. (1990). B**46**, 149–153

A Generalized Description of Ideal Crystal Structures for Monatomic Solids

BY W. L. NG

Department of Chemistry, University of Malaya, 59100 *Kuala Lumpur, Malaysia*

(*Received* 3 *July* 1989; *accepted* 27 *October* 1989)

Abstract

A variety of ideal close-packing structures were constructed using a stacking mechanism with rhombus, square and triangular nets of atoms interrelated by a common angular parameter. The structural features of the resulting space lattice are greatly influenced by the sequence and mode of stacking and the type of

0108-7681/90/020149-05$03.00